JGR Solid Earth

Key Points:
- We obtain a 3D seismic velocity model of the northern Hikurangi margin using local earthquakes recorded on land and ocean bottom seismometers
- P wave velocity model allows us to detect the approximate outline of the plate interface and continental and oceanic crustal thicknesses
- High Vp/Vs anomalies may represent high pore fluid pressures in the subducting plate that can be associated with onset of slow slip events

Seismic Velocity Heterogeneity of the Hikurangi Subduction Margin, New Zealand: Elevated Pore Pressures in a Region With Repeating Slow Slip Events

Jefferson Yarce[1,2] , Anne Sheehan[1] , Steven Roecker[3] , and Kimihiro Mochizuki[4]

[1]Cooperative Institute for Research in Environmental Sciences and Department of Geological Sciences, University of Colorado Boulder, Boulder, CO, USA, [2]Now at Department of Earth and Environmental Sciences, University of Michigan, Ann Arbor, MI, USA, [3]Rensselaer Polytechnic Institute, Troy, NY, USA, [4]Earthquake Research Institute, University of Tokyo, Tokyo, Japan

**Abstract** We investigated the seismic velocity structure of the Hikurangi margin in New Zealand to uncover the physical features of the subduction zone and explore the relationships between microearthquake seismicity, seismic velocity structure, and slow slip events. Using local earthquake tomography with data collected from both temporary ocean bottom seismometers and on-land permanent seismic stations, we used the tomography code TomoFD to iteratively perform a damped least squared inversion of absolute P and S arrival times to obtain relocated hypocenters and generate 3D velocity models for Vp and Vp/Vs. The seismic tomography images show two high Vp/Vs anomalies, one offshore and adjacent to a subducted seamount and the other beneath the North Island of New Zealand. The ~50-km wide offshore anomaly extends ~10 km beneath the plate interface and lies directly beneath the area that slipped at least 50 mm during the 2 week-long 2014 slow slip event. High Vp/Vs values may be related to high pore fluid pressures from subducted sediments, and such increases in pore fluid pressures have been suggested to trigger the occurrence of slow slip events in active subduction zones. The second onshore high Vp/Vs anomaly is located in the overlying plate and subducting slab and correlates with areas suggested by other geophysical techniques to be rich in fluids. Our seismic imaging supports interpretations that subduction processes in the Hikurangi margin are highly dependent on physical features such as subducted seamounts and fluid-rich sediments.

1. Introduction

The plate subduction boundary where the Pacific plate underthrusts the Australian plate in the North Island of New Zealand, known as the Hikurangi margin, has hosted large earthquakes and slow slip events (SSEs) that are generated as the Pacific plate converges obliquely with that part of New Zealand (Figure 1) (Wallace et al., 2004). SSEs occur when a plate interface slips over a prolonged period of days to months, moving at an accelerated pace compared to typical plate motions but substantially slower than the displacement rate of an earthquake. Global Position System (GPS) records, maintained by New Zealand's research institute GeoNet (www.geonet.org.nz), have recorded around a dozen SSEs in last 20 years with a recurrence every ~18–24 months. Unlike other worldwide examples of SSEs, the northern Hikurangi SSEs can be particularly shallow (<15 km), propagating even up to the seafloor, and do not extend throughout the entire margin but rather are limited in their spatial extent (Wallace, 2020; Wallace et al., 2016, 2017).

The northern Hikurangi margin may be unusual because the down-going Pacific plate in this region contains an oceanic plateau, the Hikurangi Plateau, forcing thicker oceanic crust, thick sedimentary sequences, and abundant seamounts into the subduction zone (Davy et al., 2008). It is possible that these features inherent to the Hikurangi Plateau contribute to or affect the seismicity and SSEs in this area, a relationship that is not fully understood yet. High resolution seismic reflection profiles and high amplitude magnetic anomalies suggest that there are variably sized subducting seamounts with locally entrained sediments in several locations along the northern Hikurangi margin (Barker et al., 2018; Bell et al., 2010; Gray et al., 2019). Subducted sediments, associated with seamounts or from other thick sedimentary and volcaniclastic sequences, have been interpreted to enable elevated pore fluid pressures that promote the shallow SSEs in this area (Ellis et al., 2015; Ito et al., 2007; Kodaira et al., 2004; Mochizuki et al., 2008). Recently, a northern Hikurangi margin SSE in September–October 2014 that accommodated plate slip equivalent to
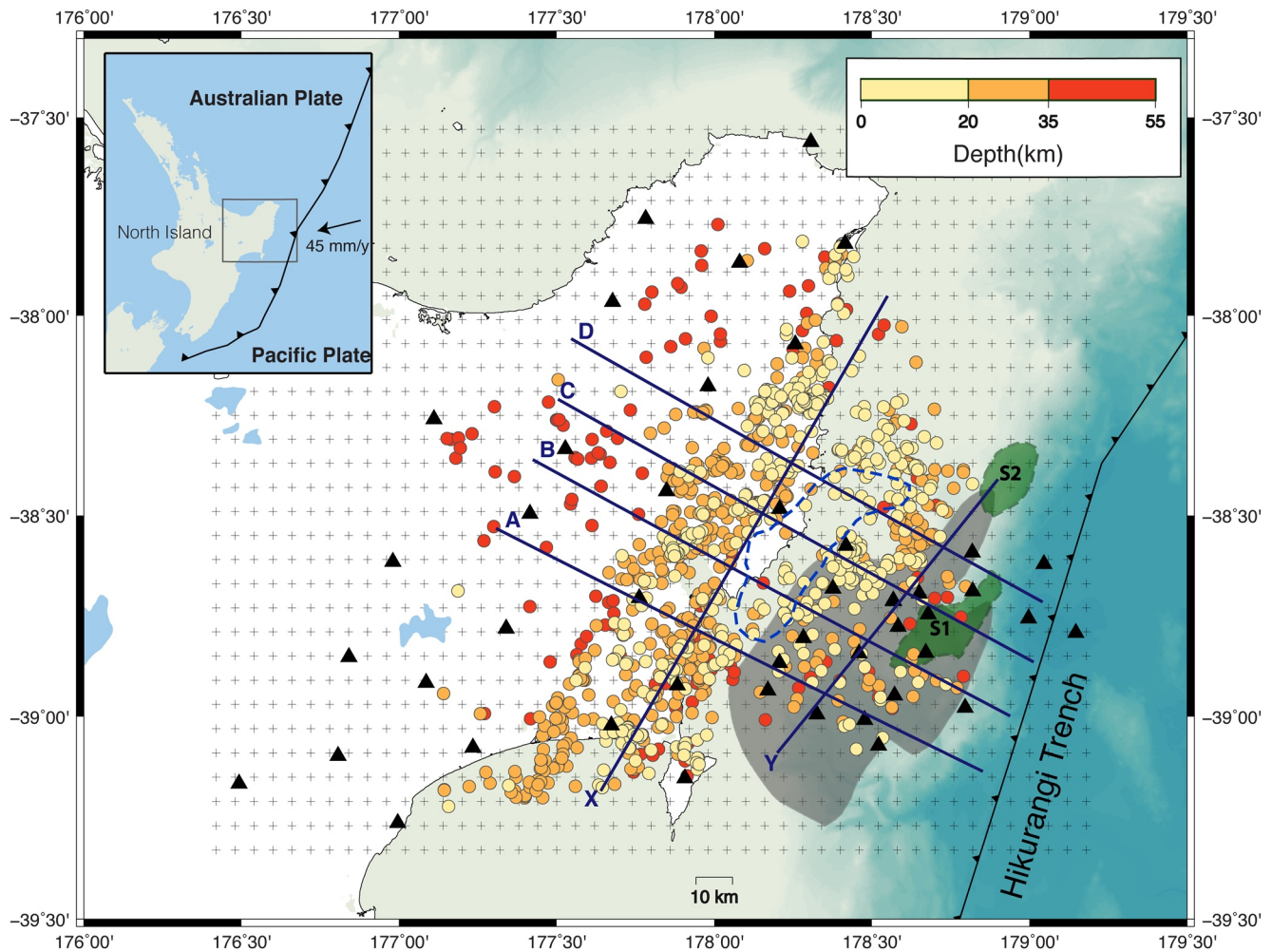
Figure 1. Location and tectonic setting of our study area. Subset catalog of earthquakes used for the tomography inversion color coded by hypocentral depth. Gray shaded area encloses the September–October 2014 slow slip area with displacement of at least 50 mm. Shaded green areas surrounded by dashed lines are locations of inferred subducted seamounts S1 (Barker et al., 2018), and S2 (Bell et al., 2010). Blue dashed line encloses the area of microearthquake seismicity gap as in Yarce et al., (2019). Coarse selection of grid nodes is shown with small gray crosses (the full grid has two nodes in between with ~2.2 km spacing). Black triangles show temporal and permanent seismometers from the Hikurangi Ocean Bottom Investigation of Tremor and Slow Slip experiment and GeoNet, respectively. Dark blue lines labeled A, B, C, D, X, and Y mark the cross sections views of seismicity and tomography images shown in Figures 3, 6, and 9. Inset map shows the location of the Hikurangi margin relative to the North Island with Pacific Plate converging with the Australian plate at 45 mm/yr.

a moment magnitude (M_W) 6.8 earthquake was proposed to be associated with fluid migration and excess pore fluid pressures within the subducted deep sediments (Shaddox & Schwartz, 2019; Todd et al., 2018; Wallace et al., 2016; Yarce et al., 2019; Zal et al., 2020).

In addition to the unclear relationship between SSEs and seismicity, the location of the Northern Hikurangi margin SSEs offshore the North Island creates another challenge to characterize the SSEs in this region. Fortunately, the September–October 2014 SSE offshore Gisborne, New Zealand was recorded by a variety of geophysical instruments as part of an interdisciplinary and international experiment, the "Hikurangi Ocean Bottom Investigation of Tremor and Slow Slip (HOBITSS)". Temporary ocean bottom pressure recorders as well as the permanent onshore GeoNet GPS network detected the SSE (Wallace et al., 2016). Additionally, broadband and short period ocean bottom seismometers (OBSs) as part of the HOBITSS experiment recorded seismic data during this event. Therefore, the available near-field data provide an opportunity to further explore the seismic behavior of a subduction boundary during SSEs.

Several studies have utilized HOBITSS data to investigate the 2014 SSE with regard to its temporal and spatial relationship to tremor (Todd et al., 2018), microearthquakes (Yarce et al., 2019), repeating earthquakes

(Shaddox & Schwartz, 2019), and temporal variations of shear wave splitting and P- to S-wave velocity (Vp/Vs) ratios (Zal et al., 2020). These investigations concluded that the presence of elevated pore fluid pressures in conjunction with the fractured subducted plate and subducted seamounts might play an important role in the location, duration, and magnitude of SSEs in this part of the Hikurangi margin. However, these studies did not show the 3D spatial distribution of suggested elevated pore fluid pressures or assess whether there are structural controls in the geometry of the slow slip area.

Use of the abundant seismicity in the subduction zone allows us to create detailed imaging of the seismic velocity and therefore tectonic structures that likely control the onset of the northern Hikurangi SSEs. Several representative seismic tomography images have been computed for the North Island of New Zealand and even specifically for the northern Hikurangi margin (e.g., Eberhart-Phillips & Bannister, 2015; Haijima, 2015), but these 3D velocity models have had limited resolution offshore due to the absence of ocean bottom seismic data. Using the newly available HOBITSS ocean bottom seismic data, we have created a 3D velocity model to determine the seismic properties of the northern Hikurangi subduction features (geometry of plate interface, subducted seamounts, relative amount of entrained sediments, and oceanic crust thickness) and analyze the relationship between these elements, SSEs, and seismicity. We integrated local earthquake P and S wave travel time data from approximately 2,000 earthquakes recorded during the year-long HOBITSS experiment. Our seismic tomography images constrain the geometry and spatial arrangement of the features, such as subducted seamounts and piles of sediments with high pore fluid pressure, in the northern Hikurangi subduction margin, ultimately yielding insight into what controls the seismicity in this area and the slow slip events in particular.

2. Data and Methods

2.1. Earthquake Catalog

The primary seismic data for our tomographic velocity inversion derives from a catalog of earthquake arrival times in the northern Hikurangi margin (Yarce et al., 2019). These arrival times were manually picked to assemble a catalog of hypocenters using ocean bottom and land seismometers with station spacing ranging from 6 to 38 km for the combine network (average spacing of 19 km). For this tomographic study, we selected a subset of 1,172 local earthquakes from the catalog that had at least 8 phase arrivals with a minimum of two S-wave picks to enhance location accuracy. We further restricted our selection of events to those with an azimuthal gap in station coverage of less than 180 degrees so that all of the hypocenters were within the aperture of the recording stations. This subcatalog of earthquakes includes 20,760 handpicked arrival times with 10,379 P- and 10,381 S-phase picks. On average, P- and S-wave arrival times are uncertain to 0.08 and 0.10 s, respectively, with uncertainties assigned manually during picking (Yarce et al., 2019) and further constrained during manual reassessment of 200 P- and 100 S-wave arrivals chosen randomly. The selected earthquakes range in local magnitude (M_L) between 0.2–4.7 and in depth from 1.4 to 70.7 km below sea level. When plotted, this earthquake subset reveals a spatial distribution of seismicity similar to the one presented in Yarce et al. (2019), confirming the subcatalog used for tomographic inversion is representative of the regional seismicity (Figure 1).

2.2. Tomography Method

We use this subcatalog of P- and S-wave earthquake arrival time data in a tomographic inversion to solve for the 3D velocity structure in the northern Hikurangi margin. We used the finite-difference tomographic inversion method (TomoFD) developed by Roecker et al. (2006, 2017), which inverts P- and S-wave arrival times to solve iteratively and simultaneously for earthquake hypocenters, P-wave velocity structure, and Vp/Vs ratios. This algorithm makes use of a finite-difference solution to the eikonal equation to generate travel times in a volume of nodes to calculate travel time residuals (Hole & Zelt, 1995; Vidale, 1988), adapted to a spherical (Earth-centered) coordinate system (Li et al., 2009; Zhang et al., 2012). The finite difference method has several advantages over standard ray tracing, including improved determination of global travel time minima and better accuracy in complex tectonic settings, as anticipated for the Hikurangi subduction zone (Roecker et al., 2006). TomoFD has been previously used in other regions with strongly heterogeneous

media such as San Andreas fault (Roecker et al., 2006), volcanic systems in Iceland (Greenfield et al., 2016; Schuler et al., 2015), and the Andean subduction zone (Comte et al., 2019).

The resulting velocity model depends on station distribution, grid node spacing in a spherical section, and the initial velocity model. The HOBITSS array together with the selected GeoNet stations consists of a network of seismometers with spacing between 6 and 38 km (Yarce et al., 2019). We built a spherical grid that encloses the seismometer network and epicenters and down to 96 km depth to include the turning points of rays from the deepest hypocenters of the selected catalog of earthquakes. Horizontal spacing of nodes are constant at 0.02° (~1.74 km for this latitude) in longitude and latitude, while depth spacing is set to 2 km (Figure 1). Despite not varying independently, this fine node spacing lessens the dependence of the final model on the location of the grid points (Roecker et al., 2006).

Hypocenters and wave velocities are estimated by iteratively solving linear approximations to nonlinear equations that relate them to the observations (arrival times). We regularize this procedure in two ways: first by adapting a standard damped least squares approach, and second by a posteriori smoothing of perturbations at each iteration with a moving average window. The damper prevents large perturbations at any single iteration, and the moving average window mitigates the appearance of artifacts in the model that are smaller than the resolution capabilities of the data set. These steps are taken to generate a simple or "smooth" model that adequately explains the observations.

Although the smoothing is performed after inversion, this operation smooths the perturbations to the model rather than the model itself. Additionally, this a posteriori smoothing does not result in a solution less optimal than a solution with regularized least squares inversion that appends a more conventional Laplacian smoothing matrix as a constraint (Roecker et al., 2006). This smoothing procedure has two advantages: (1) it produces similar results to the spatial regularization with an inverse covariance matrix (or a Laplacian smoothing matrix, which is a simple way to achieve a similar outcome), but with much less computational effort; and (2) it effectively mitigates the appearance of short wavelength features at initial iterations, which, once they appear, tend to persist even if they are not required by the observations. The efficacy of this smoothing procedure lies in the iterative solution nature of our approach.

The choices of damper and moving window length are somewhat arbitrary but are governed by the same resolution versus covariance considerations used to find an optimal damper in linear or single iteration least squares inversions (e.g., Aki & Richards, 1980). Hence, it is useful to explore the consequences of various choices of damper and moving average window length on the resulting model.

We note that TomoFD solves the system of linear equations with the LSQR algorithm of Paige and Saunders (1982), which uses a single damping parameter for all variables. Since we solve for variables with different units (e.g., km/s for P wave speeds and a dimensionless Vp/Vs ratio) we apply a column-wise scaling based on the relative sizes of the diagonals of the normal equations. For our purposes, a scaling factor of 10 was used to calibrate the diagonals of the Vp and Vp/Vs ratios.

We determined optimal damping and smoothing parameters by observing the trade-off between calculated data variance and roughness (or model complexity) over different ranges of values for damping and smoothing parameters, while also monitoring the number of iterations. Following Greenfield et al. (2016), we define roughness as the root-mean-square of the second spatial derivative of the model. We tested Vp damping values between 2 and 200 and three different smoothing parameters: A 5 node (vertical) by 7 node (horizontal) moving average, a 5 node by 5 node moving average, and a 3 node by 3 node moving average. Given the uncertainties of 0.08 and 0.10 s for P and S arrival times (Yarce et al., 2019), the variance in P and S wave residuals was expected to be greater than 0.006 and 0.010 s², respectively, with variances below these noise levels signaling an overfitting of the inversions. Applying a smoothing parameter of $3 \times 3 \times 3$ nodes resulted in variances below the expected noise levels and overall model complexities 3 to 4 times larger than the other two smoothing parameters tested (Figure S1a). However, smoothing parameters of $5 \times 5 \times 5$ nodes (Figure S1b) and $7 \times 7 \times 5$ nodes (Figure S1c) produced models with similar roughness and variance responses. In such cases, it is considered preferable to use the smoother model (Greenfield et al., 2016) and so we chose to use the $7 \times 7 \times 5$ smoothing. Damping values between 2 and 20 tended to generate overly rough models, while values greater than 50 produced models of the same degree of roughness; the main difference being in the number of iterations required to produce the same result (Figures 2 and S1). We therefore consider a damping value of 50 and
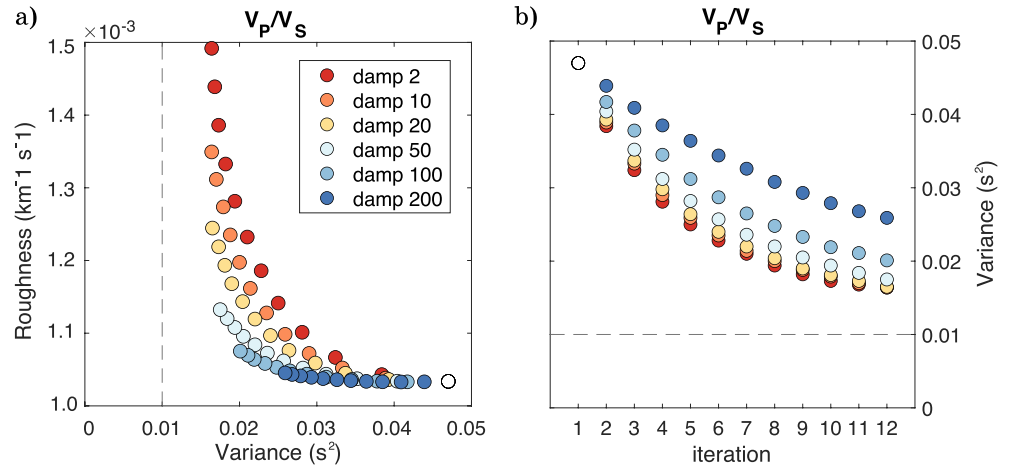
Figure 2. Variance of data for 12 iterations for 6 different damping values showing constant reduction of variance through 12 iterations for Vp/Vs models. (a) Changes in variance of the data relative to model roughness for each Vp/Vs model for a range of damping values between 2 and 200. Every circle represents an iteration of the model relative to the color-coded damping. Iterations increase from right to left for runs up to 12 iterations (white circle marks iteration 1). (b) Changes of variance observed after each iteration. These results correspond to the selected smoothing parameter of 5 vertical nodes and 7 horizontal nodes of smoothing moving average. For other smoothing parameters please refer to supplemental material (Figure S1). These runs were performed under same parameter conditions (except for the changing damping) and for a unique data set under very flexible constraints in travel time residual threshold and standard deviations. Gray dashed lines indicate the expected variance given the uncertainties in arrival time data with 0.010 s^2 for S arrivals.

a moving average window of $7 \times 7 \times 5$ nodes as providing the best trade-off between roughness and misfit of data (Figure 2 and Table 1). Our preferred model was obtained after 12 iterations, at which point residual variances of 0.012 and 0.027 s^2 for P- and S-wave were obtained. Representing a ~63% reduction for P residual variance and a 60% for S residual variance relative to our 3D starting model.

In generating a starting model, we incorporated the 3D velocity model of Eberhart-Phillips and Bannister (2015), who produced a 3D velocity model of this region using data from permanent and temporary land seismometer networks as well as shot gathers from an offshore active source marine seismic survey. While this type of a priori information is a definite advantage, the sensitivity of our result to the choice of starting model should be demonstrated, and to do so we considered the effects on the inversion when using two different 1D velocity models for onshore and offshore Hikurangi margin, after Yarce et al. (2019).

To test for possible biases stemming from our choice of an initial 3D velocity model, we performed inversions with the parameters explained above (damping of 50, smoothing of $7 \times 7 \times 5$, and for 12 iterations), with two independent 1D velocity models. While the 1D-based inversions had different absolute values of P wave velocities, we determined that its relative spatial pattern remains similar to the inversion performed using a 3D starting velocity model. Notably, the general locations of high Vp/Vs anomalies (defined as regions where Vp/Vs > 1.83, HK1 and HK2) are consistent with all three starting models (one 3D and two 1D) (Figure S2). We note there are substantial velocity heterogeneities within the HK2 anomaly. The variances of body wave arrival time residuals calculated from the 1D onshore and offshore starting models are significantly higher (0.055 and 0.074 s^2, respectively) than those found using our preferred 3D model (0.018 s^2) (Figure 2). We infer that while the patterns in

Table 1
Summary of Body Wave Variance (a) and Model Roughness (b) for Iteration 12 for the Range of Damping and Smoothing Parameters Tested

	Variance (s^2)		
(a)		Smoothing	
Damping	$7 \times 7 \times 5$	$5 \times 5 \times 5$	$3 \times 3 \times 3$
2	0.0164	0.0144	0.0108
10	0.0164	0.0132	0.0086
20	0.0165	0.0131	0.0079
50	0.0175	0.0141	0.0085
100	0.0201	0.0164	0.0106
200	0.0259	0.0224	0.0153
	Roughness ($km^{-1} s^{-1}$) $\times 10^{-3}$		
(b)		Smoothing	
Damping	$7 \times 7 \times 5$	$5 \times 5 \times 5$	$3 \times 3 \times 3$
2	1.49	2.04	6.01
10	1.35	1.75	4.82
20	1.24	1.53	3.80
50	1.13	1.28	2.54
100	1.08	1.15	1.89
200	1.05	1.08	1.46
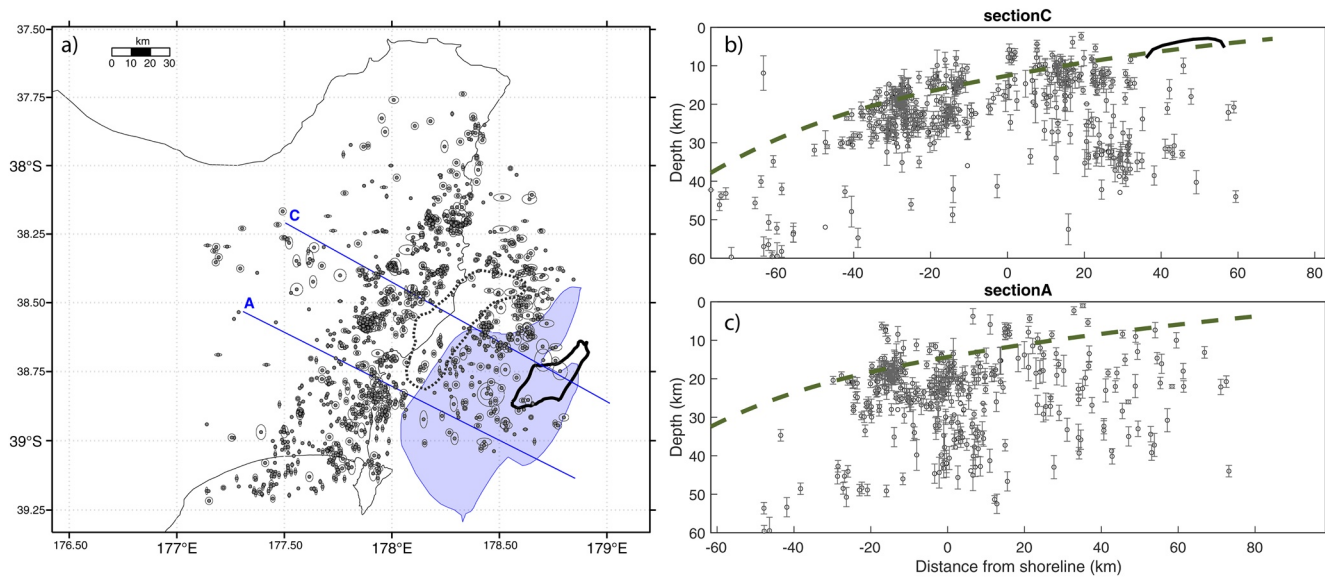
Figure 3. Hypocenter locations in map and cross-sectional views. (a) Gray circles with black edges show earthquakes used for tomographic inversion with ellipses representing the horizontal uncertainty. Dark blue lines show cross sections in (b and c). Black dashed line outlines the microearthquake seismicity gap from Yarce et al. (2019). Blue shaded area is the 50 mm 2014 SSE displacement contour from Wallace et al. (2016). Black bold line encloses the subducted seamount from Barker et al. (2018). Panels (b and c) are seismicity cross sections of earthquakes within 20 km of the lines indicated in (a); error bars of earthquake depth shown in gray. Dark green dashed line is the interface from Williams et al. (2013). Black bold line in (b) outlines the projection of the subducted seamount shown in (a).

velocities are robust and insensitive to the starting model, the absolute values obtained from the 3D starting model provide a better representation for this portion of the Hikurangi margin

3. Results

Our hypocenters (Figure 3) relocated with the 3D model show a gap in seismicity in the same area documented by Yarce et al. (2019). This gap is roughly parallel to the coast and spans a region ~55 km in length and ~20 km wide. The distribution of seismicity from this 3D study is similar but not identical to that found using a 1D velocity model (Yarce et al., 2019). Hypocenter relocations are an average of 5 km of epicentral distance from those of the original data set, with a median azimuthal change of 251° (meaning that the relocated events are typically located landward of the starting locations), and with depth changes averaging 2.8 km shallower than the 1D relocations (Figure S3). Much of the offshore seismicity seaward from the seismicity gap is now located much closer to the plate interface (Figure 3, interface shown as green dashed line). Onshore seismicity is mainly confined to the upper 10 km of the down-going plate, showing an intraplate distribution. However, Section D also has seismicity in the overlying plate with seismicity between 10 and 20 km below sea level (see Figure 6).

The P-wave velocity distribution and Vp/Vs ratios across our study area offers insights into the geometry of the plate interface and heterogeneities throughout the subduction margin (Figures 4–6). The 3D P-wave velocity model is smooth with gradual transitions from slower to faster velocities with depth (Figures 4 and 6a). Transitions of velocities from 5 to 6 km/s over a small depth interval roughly coincides with the offshore subduction interface of Williams et al. (2013). On land, the transition from 5 to 6 km/s is more broadly distributed across the nearly ~30 km thick overlying crust (Stern et al., 2010).

In contrast to the relatively smooth Vp model, the 3D Vp/Vs ratios vary substantially along both the strike and dip of the subducting plate (Figures 5 and 6b). In sections B–D that traverse the microearthquake seismicity gap near the shoreline (gap indicated by dark blue line parallel to interface in Figure 6b), the oceanic crust of the subducting plate shows intermediate Vp/Vs values around 1.74 to 1.8. East of the gap and seawards, there is a high Vp/Vs anomaly (Vp/Vs > 1.83) that is found consistently in all cross sections (HK1 in Figures 5 and 6b). Using magnetic and seismic reflection data, a subducted seamount was previously
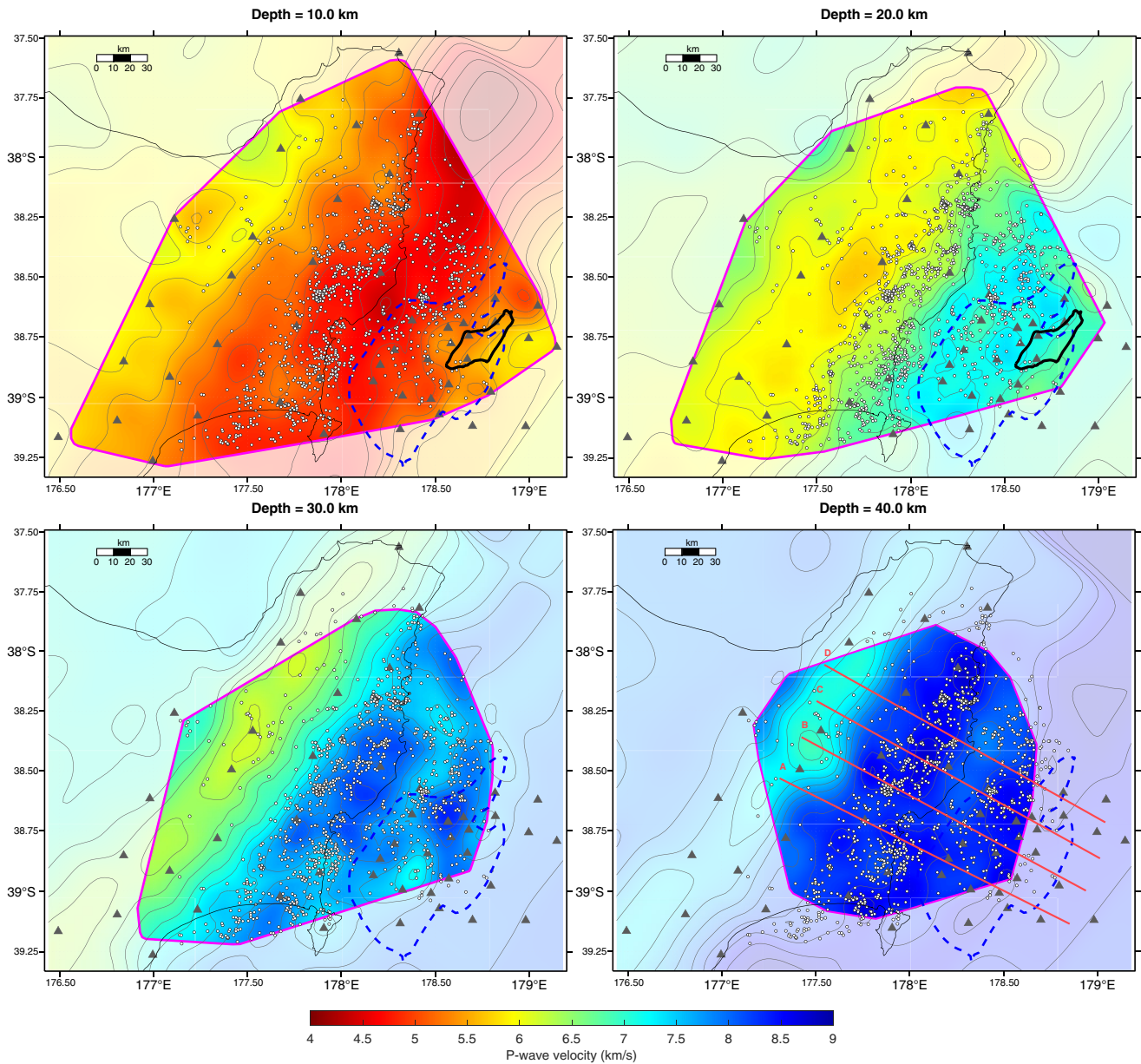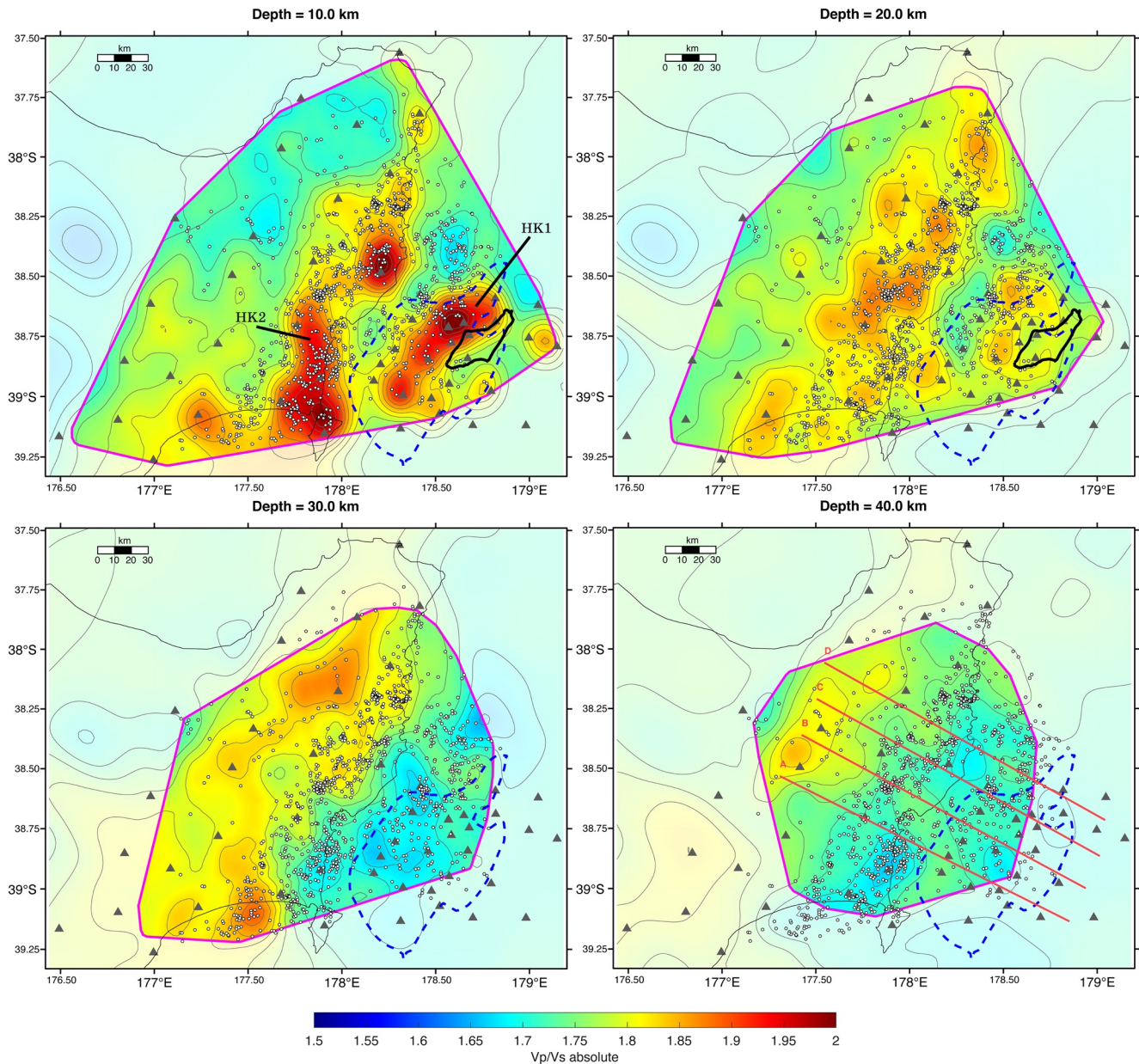
Figure 4. Map views and inversion results for Vp at depths 10, 20, 30, and 40 km. Vp contour interval 0.2 km/s. Magenta line limits the area with nodes with at least 10 in the hit count. Location of 2014 SSE (dark blue dashed line), and seamounts (black line). White circles represent epicenter locations of relocated earthquakes.

inferred just east of this Vp/Vs anomaly by Barker et al. (2018) and sections B–D should cross this seamount. Another high Vp/Vs anomaly (HK2) towards the west and inland, is revealed in both the overlying plate and in the down-going plate (Figure 6b). Between 30 and 40 km depth, there is also a patch of low Vp/Vs in the down-going plate that appears in all cross sections at approximately −10 to 40 km from the shoreline. However, the lower resolution at these depths makes this feature less certain.

We find that earthquake hypocenters are concentrated in and slightly downdip of regions with high Vp/Vs ratios. Up-dip from the seismicity gap, hypocenters are concentrated at the transition from a Vp/Vs of ~1.75 to as much as 1.85 (HK1 in Figures 3 and 6b). Down-dip from the gap, seismicity in the four cross-sections extends over the overlying crust and down-going crust with Vp/Vs ratios >1.8, corresponding with the high Vp/Vs anomaly labeled HK2 in Figures 3 and 6b.

Figure 5. Map views and inversion results for Vp/Vs ratios at depths 10, 20, 30, and 40 km. Vp/Vs contour interval every 0.05 change in ratio. Magenta line limits the area with nodes with at least 10 in the hit count. Location of 2014 SSE (dark blue dashed line), and seamounts (black line). White circles represent epicenter locations of relocated earthquakes.

4. Model Resolution and Synthetic Tests

We constructed checkerboard tests to assess the resolving power of our arrival time data set. This typical procedure perturbs a background velocity model representative of the area, generates synthetic seismic data, and then attempts to recreate the artificial velocity anomalies with the identical procedure used with real data. We conducted two different types of checkerboard tests to understand the geometry and resolvable size of anomalies: (1) alternating $\pm 5\%$ perturbations in prisms that are approximately $8.7 \times 8.7 \times 10 \ km^3$ (or 5 consecutive nodes in the horizontal plane and 5 consecutive nodes in vertical), with perturbed prisms separated by regions of the same size with no perturbation (Figure 7). (2) A finer version of the first test with 3 consecutive nodes instead of 5 to examine whether smaller-scale anomalies ($\sim 5.2 \times 5.2 \times 6 \ km^3$)
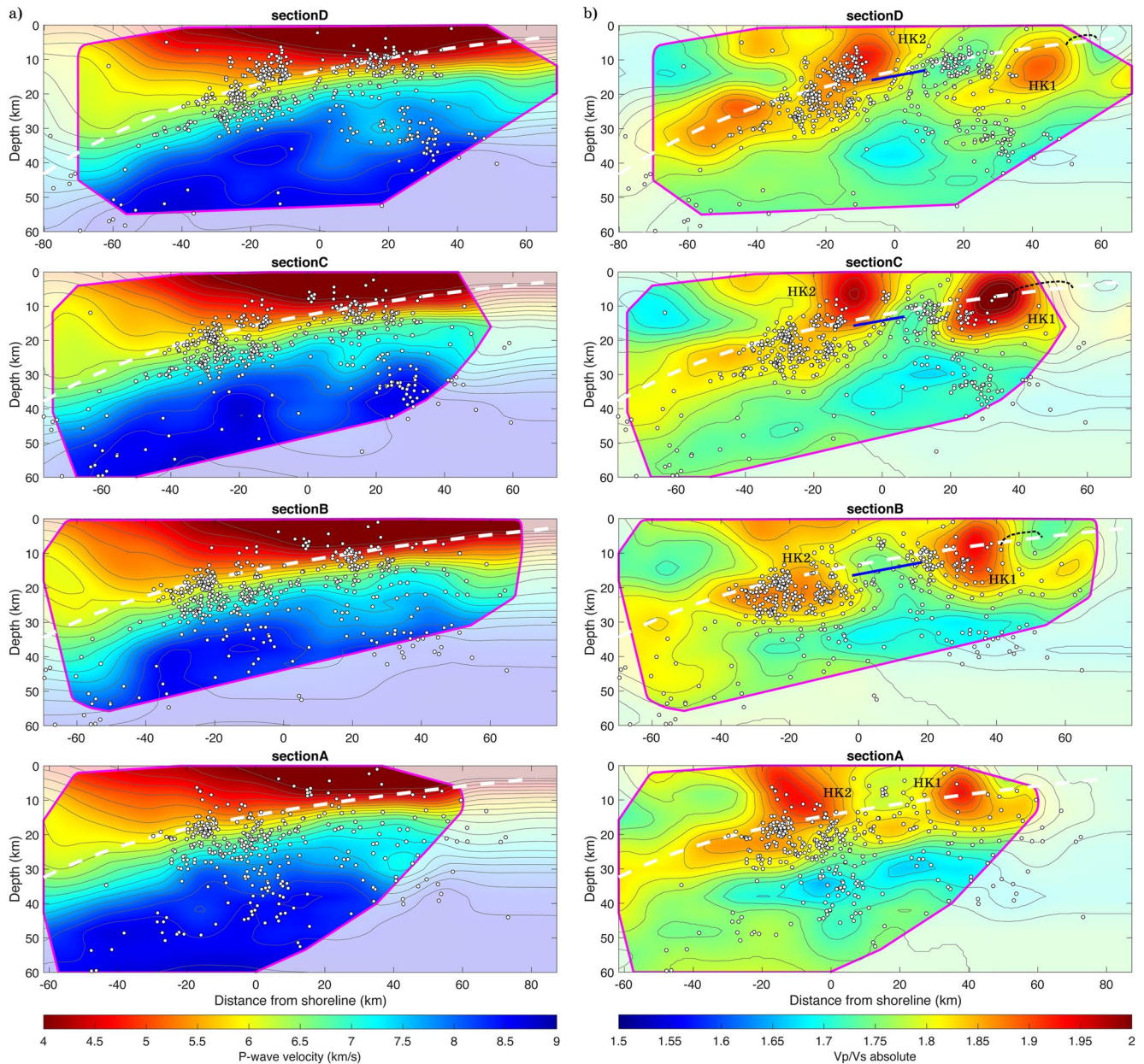
Figure 6. Vertical cross-sections of the 3D Vp (a) and Vp/Vs (b) models. Magenta line limits the area with nodes with at least 10 in the hit count. White dashed line denotes plate interface from Williams et al. (2013). Black dashed line marks the location of the subducted seamount shown in Figure 4. Dark blue line parallel to interface indicates the location of microearthquake seismicity gap. White circles represent hypocenter locations of relocated earthquakes.

would be detectable in our 3D velocity model (Figure S4). In both cases we use a 1D velocity model as the background.

The two checkerboard tests show that the inversion is able to recover velocity features within the aperture of the seismic network and for depths between 2 and 40 km. These areas, outlined by the green line in Figure 7, correspond to nodes with at least 10 ray hits. The checkerboard tests further suggest that the tomographic inversion can resolve ±5% Vp features that are at least ~$8.7 \times 8.7 \times 10$ km^3 ($5 \times 5 \times 5$ nodes), within the well resolved area. The finer checkerboard test with 3 consecutive nodes perturbed in every direction was able to partially recover some areas around the center of the array and for shallower depths (between 2 and 25 km) than the $5 \times 5 \times 5$ checkerboard (Figure S4). However, the region of finer scale checkerboard resolution is much more limited than the coarser checkerboard.
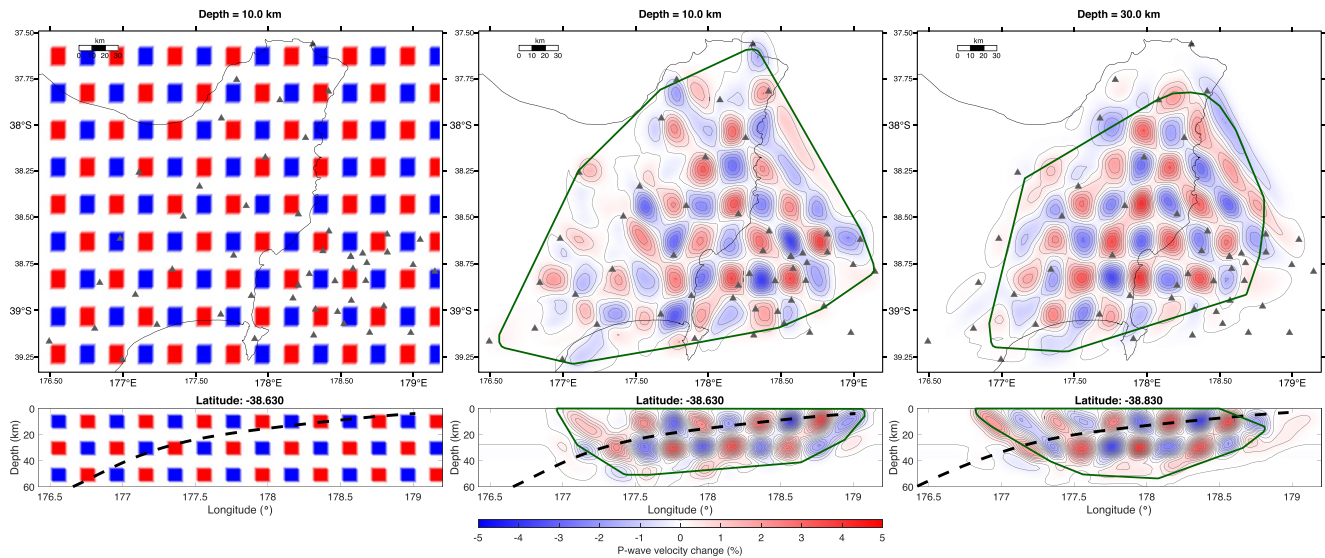
Figure 7. Checkerboard resolution tests for perturbations of ±5% from a 1D velocity model representative of the study area, prisms include 5 consecutive nodes in the horizontal and vertical axis. Left panel shows map (top) and cross-sectional views (bottom) of the initial perturbation of the 1D velocity model. Results of inverting the synthetic data under these perturbations (center and right). Top of center and right panels show results of recovery at 10 and 30 km depth. Bottom of center and right panels show cross sectional recoveries at latitudes −38.63° and −38.83°. Green outline in map and cross sections denotes the area with nodes with hit count at least 10. Black dashed line in lower panels denotes plate interface from Williams et al. (2013).

To investigate the effects of data uncertainties on resolution, we added noise to the calculated travel times of the synthetic data of over a range of ±0.10 s for P arrivals and ±0.15 s for S arrivals. These values are slightly larger than the reported pick uncertainties to ensure that the noise is effectively represented. Noise was assumed to be normally distributed with both 1-sigma (Figure S5) and 2-sigma (Figure S6) deviations. In a third synthetic data set, we added random noise that equals the final standard deviation determined for the actual arrival times (Figure S7). Comparing the recovery of the checkerboard tests in each case shows that the checkerboard patterns with added noise were well recovered (Figures S5–S7). Given these results, we argue that our images are robust to levels of noise that are up to 2 standard deviations greater than the expected noise level.

While checkerboard analysis is a standard and common way to evaluate seismic tomography images, the capability to solve for the nonuniqueness of the inversion is an insufficient assessment of the quality and reliability of the model (e.g., Rawlinson et al., 2014; Rawlinson & Spakman, 2016). An alternative synthetic reconstruction test (Prevot et al., 1980) attempts to recover specific anomalies found in the preferred model. Using this "realistic feature" test, we assessed the detection of synthetic structures with heterogeneous shapes that mimic the high Vp/Vs anomalies (HK1 and HK2) found in our image, specifically those anomalies around the subducting interface, between 4 and 28 km depth (see Figures 8a and S8–S18).

We performed a total of six of these feature tests that modeled those high Vp/Vs anomalies in different ways and with slightly different geometries to test if our ray set had the ability to resolve such structures with those geometries and positions (summarized in Table 2). First, in a test we call FT1, synthetic data were produced with two anomalies of 5% faster velocity in P wave and no alteration in S wave velocity (thus, Vp/Vs increases with Vp). Second, in experiment FT2, synthetic data were created that contained the two anomalies with 5% faster velocities in both P and S wave velocities (thus Vp/Vs should remain unaltered from our preferred velocity model). Third, in test FT3, we set up two anomalies with 5% larger Vp/Vs ratios through unperturbed Vp velocities but 5% slower Versus because the geology of the overriding plate is inherently different from the underlying plate and there can be smearing effects in the tomographic inversion, we explored if we could resolve whether Vp/Vs anomalies residing in both plates, only in the overlying plate, or only in the underthrusting plate in our FT4 and FT5 tests. In a final test (FT6), we assessed the possibility that our imaged HK1 and HK2 anomalies were actually a single laterally continuous structure, considering that the separation between these two could be an artifact produced by poor ray coverage.
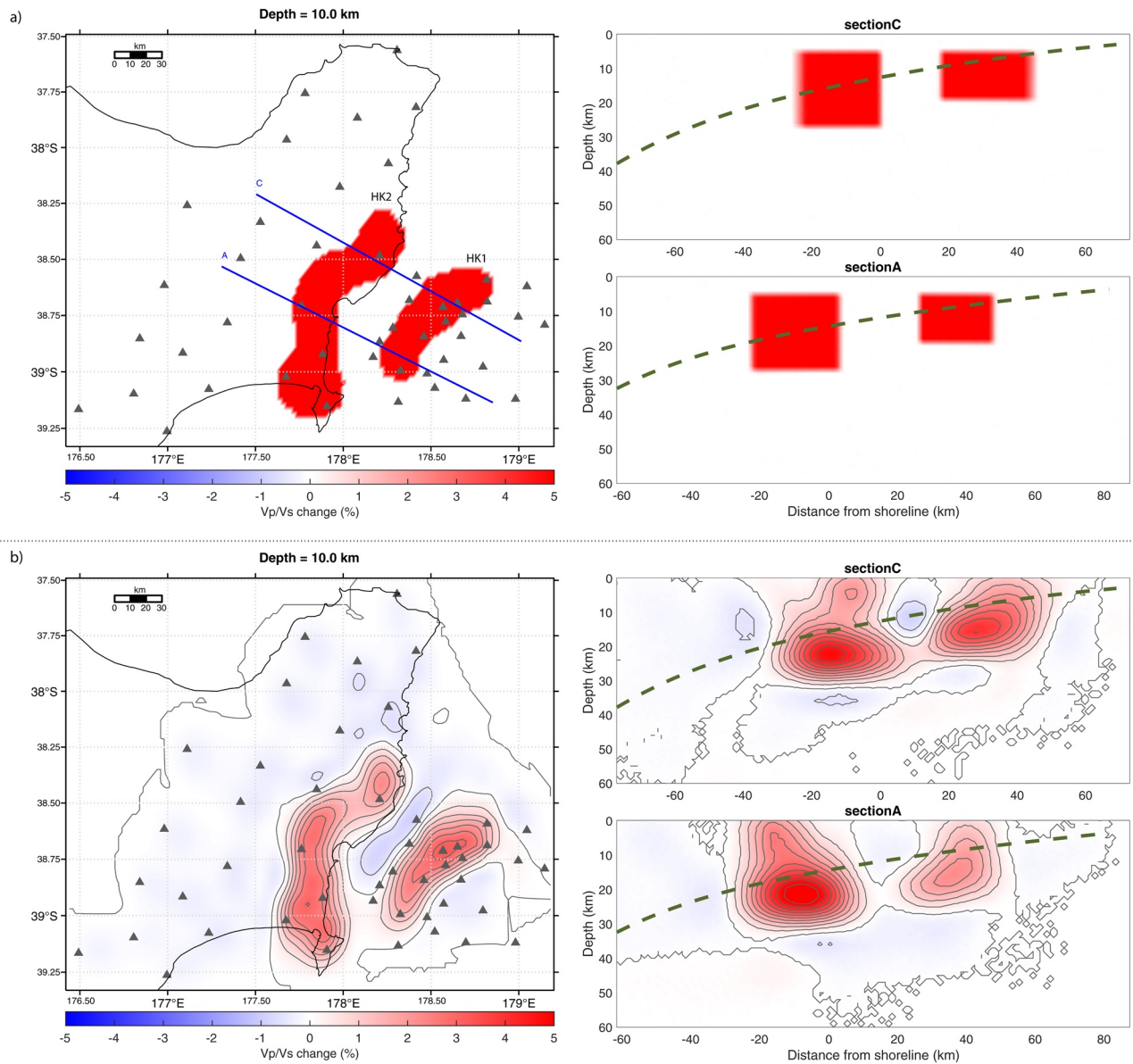
Figure 8. Feature Test 1 (FT1) Vp/Vs ratio anomaly (a) Input velocity perturbation of +5% P wave velocity for two anomalies (HK1 and HK2). (b) Resulting recovery perturbations of synthetic travel times of the perturbations in (a). Map (left) and cross-sectional views of lines A and C (right) are presented. Black dashed line in panels to right denotes plate interface from Williams et al. (2013).

We tested the recovery of Vp and Vp/Vs using various synthetic perturbations of multiple geometries to help evaluate the robustness of our model. FT1, FT2, and FT3 targeted the same shape of the HK1 and HK2 structures with perturbations of different parameters (Vp, vs., Vp/Vs). We found that those anomalies are well recovered (Figures S8–S12). However, when evaluating whether these structures could be resolved to lie in both or either the overlying plate or subducting plate, we observed that our data set is not capable of identifying an HK1 anomaly located in the overlying plate, while HK2 can be recovered and resolved by our data set in both the overlying plate and subducting plate (Figures S13–S16). Our FT6 test considered the likelihood that the separation between HK1 and HK2 is an artifact due to poor ray coverage. Here, we found that a synthetic anomaly that resembles a laterally continuous feature is fully recovered, suggesting that HK1 and HK2 are indeed separate anomalies (Figures S17 and S18). When evaluating whether the parameters that were not perturbed during these tests (e.g., vs. in FT1 or Vp/Vs in FT2) showed any major deviation, we observed that the anomalies in the recovery plots were less than ±1%. This very low detected

Table 2
Summary of Feature Test With Parameters Perturbated and Broad Description of Geometry. "--" Indicates That the Parameter in Unperturbed

|	Vp	Vs	Vp/Vs	Depth extension (km)	
				HK1	HK2
FT1 Figures 8 and S8	+5%	--	+5%	From 4 to 20	From 4 to 28
FT2 Figures S9 and S10	+5%	+5%	--	From 4 to 20	From 4 to 28
FT3 Figures S11 and S12	--	−5%	+5%	From 4 to 20	From 4 to 28
FT4 Figures S13 and S14	+5%	--	+5%	From 4 to Interface	From 4 to Interface
FT5 Figures S15 and S16	+5%	--	+5%	From interface to 20	From interface to 28
FT6 Figures S17 and S18	+5%	--	+5%	15 km thick laterally continuous anomaly	

change in unperturbed parameters may indicate that the synthetic perturbations were constrained to solely the chosen velocity or velocity ratio (Figure S19). In summary, the high Vp/Vs anomalies from our seismic tomography inversion, with dimensions of at least 11 km in each dimension, and for areas located within the green lines in Figure 7, are sufficiently robust to be interpreted as reliable features of the subduction margin.

5. Discussion

In the Hikurangi margin there is strong evidence for seamounts that have subducted, bringing along with them entrained sediment that can develop elevated porosities possibly containing high pore fluid pressures (Barker et al., 2018; Bell et al., 2010; Ellis et al., 2015). Subduction of seamounts causes widespread faulting and fracturing in the upper plate (Wang & Bilek, 2011), which consequently increases the crack porosity through the upper plate and along the interface (Sun et al., 2020). In subduction zones, deep fluids are suggested to facilitate SSE activity (Bürgmann, 2018). The presence of pores at high pressure result in variations of interactions between the overlying and down-going plates along strike, that may result in the onset of SSEs. Seismic velocities, and especially Vp/Vs ratios, are sensitive to fluid-saturated porosity (Berryman et al., 2002; Brantut & David, 2019; Christensen, 1984; O'Connell & Budiansky, 1974), and thus our model results can identify regions with potential fluid-saturated pores and help us understand the relationship between geological features and the subduction process more broadly.

With our seismic velocity model we are able to add constraints to previously reported velocity anomalies (such as HK2, identified by Eberhart-Phillips and Bannister (2015)) as well as find other anomalies (such as HK1) that are newly visible by virtue of observations from OBSs. We also find that the occurrence and spatial extent of high Vp/Vs anomalies (HK1 and HK2) are spatially associated with the occurrence of SSEs in the study area and subducted seamounts and sediments. Furthermore, the hypocenter distribution of microearthquake seismicity in the year long HOBITSS experiment is very similar to that reported in Yarce et al. (2019), with the observed seismicity gap located at a slight offset from these Vp/Vs anomalies. While the Vp model reveals the geometry of the subducting interface and overlying crustal thickness, Vp/Vs ratios show dramatic variations along strike and dip of the subducting and overlying plate.

Our results show a Vp structure that is relatively smooth and outlines the offshore interface between the subducting slab and the overlying plate. Our Vp model shows a sharp velocity gradient consistent with the plate interface of Williams et al. (2013), showing a clear boundary between the subducting Hikurangi Plateau and the overlying plate, especially in the offshore portion. Rather than hosting most seismicity along the plate interface as in most subduction zones, Hikurangi microearthquakes are hosted in the top 12–15 km of the subducting slab, interpreted as the crustal portion of the subducted slab. Additionally, the Vp distribution suggests that the subducting slab has an average crustal thickness of ∼12 km (identified by velocities between 5 and 7.2 km/s following estimates from Condie (2016) and Mooney et al. (1998) of oceanic crust seismic velocities of the upper and lower portions of the crust; Figure 6a). This thickness is also consistent with that of the Hikurangi Plateau at the southern end of the margin as revealed by a seismic survey (Mochizuki et al., 2019). Closer to the trench, at around 40 km from the shoreline, this velocity
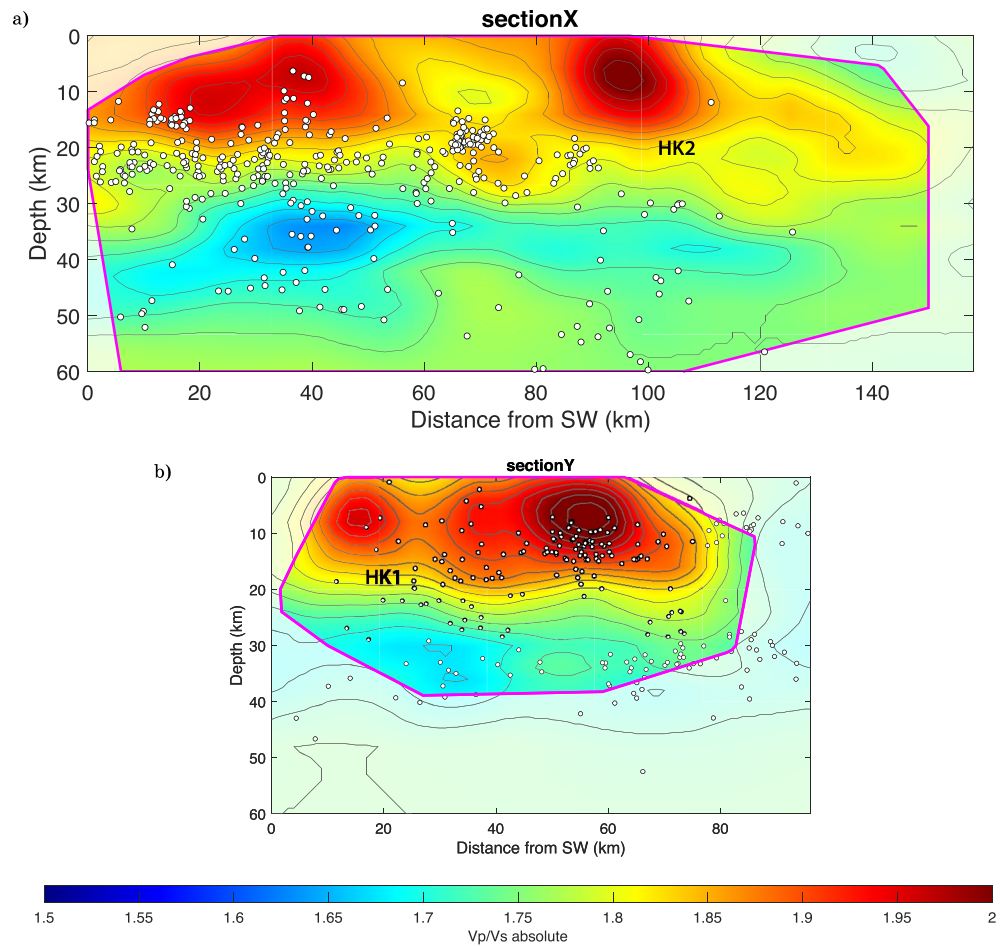
Figure 9. SW-NE cross sectional views of Vp/Vs ratio model. High Vp/Vs anomalies labeled HK1 (b) and HK2 (a).

range for oceanic crustal velocities (between 4.5 and 7.2 km/s) deepens, suggesting a thicker oceanic crust of ~15 km. This thickness is slighter higher than mean oceanic crust but is consistent with a thicker oceanic plateau such as the Hikurangi plateau (Condie, 2016; Kerr, 2003).

The Vp/Vs model displays more heterogeneity than the Vp model, likely due to the enhanced sensitivity of Vp/Vs to porosity and fluids. We find two high Vp/Vs anomalies, one located offshore and one onshore (HK1 and HK2 in Figures 5 and 6b). The onshore high Vp/Vs anomaly (HK2 Vp/Vs > 1.83) is located downdip from the microearthquake seismicity gap, between ~−50 to 0 km onshore (Figure 6b). HK2 is situated along and above the plate interface at depths between 4 and 28 km. In this area, this anomaly appears to reside in both the overlying crust and in the uppermost portion of the subducting slab, coinciding with areas of abundant seismicity (Figure 6b). Resolution tests (discussed above) show that these Vp/Vs anomalies can be found in both the overlying plate and the subducting slab. Our image of HK2 is consistent with that found by previous tomography of the Hikurangi margin, which also showed a 70-km-long high Vp/Vs anomaly in this area (Eberhart-Phillips & Bannister, 2015). In our model, we observe that the anomaly may exceed 100 km along strike (Figure 9a). Eberhart-Phillips and Bannister (2015) interpreted this anomaly as a thick sedimentary sequence in the accretionary wedge with high fluid pressure. Other evidence for the presence of fluids in this locale derive from magnetotellurics surveys showing high conductivity (low resistivity) in a very similar location or close to HK2 (Heise et al., 2017). Additionally, in a 3D seismic attenuation study of this region, Nakai et al. (2021) found that our onshore high Vp/Vs anomaly correlates spatially with a region of high attenuation (low Qs). In agreement with earlier work, we also favor a high pore fluid presence in this region beneath the North Island of New Zealand, potentially suggesting an exceptionally thick package of fluid-rich and highly fractured sediments and slab.
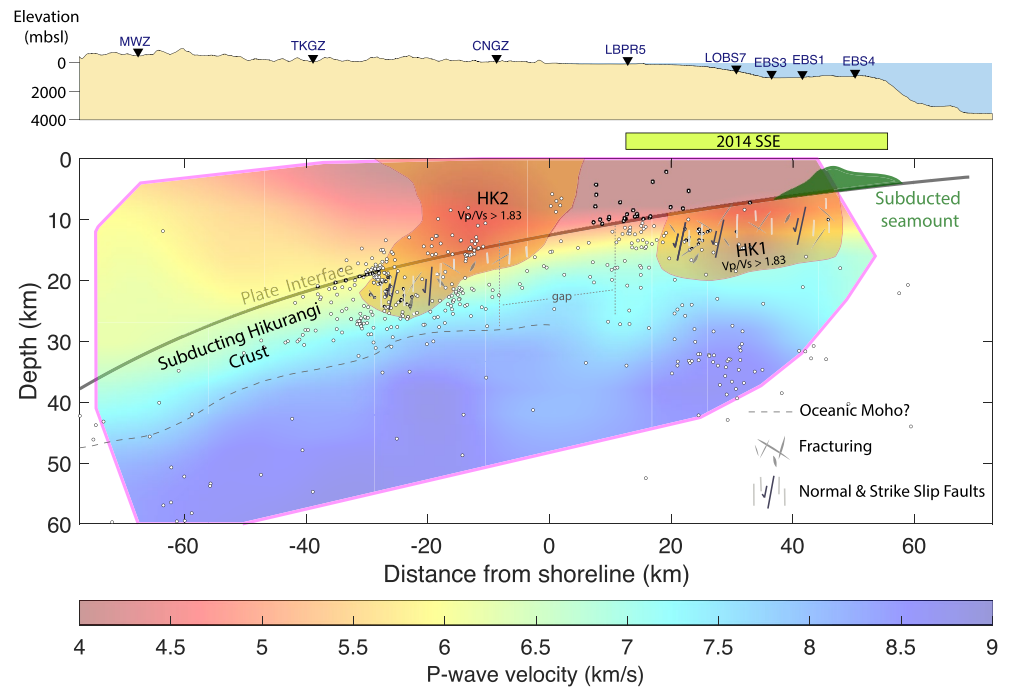
Figure 10. Schematic interpretation of the shallow subduction environment along section C. Background is a lightened version of the Vp velocity model. The schematic includes the outline of plate interface from Williams et al. (2013), interpretation of oceanic moho based on the 8.0 km/s contour line of Vp velocity model (dashed gray line), highVp/Vs anomalies HK1 and HK2 (Vp/Vs > 1.83). Possible fracturing of the subducting plate which is related to seismicity, outline of subducted seamount based on Barker et al. (2018), microearthquake seismicity gap from initial catalog used in this inversion (Yarce et al., 2019), and the location of 2014 SSE (Wallace et al., 2016).

The offshore high Vp/Vs anomaly (HK1, Vp/Vs ratios of >1.83) is likely another region of elevated pore pressures with an along strike length of ~60 km (Figure 9b). This anomaly appears in both the overlying crust and the subducting slab; however, according to our feature tests, our data is capable of resolving an anomaly in the position of HK1 only in the subducting plate but not in the overlying plate. This anomaly also overlaps with a high seismic attenuation anomaly (very low Qp and Qs) found using a subset of the earthquake catalog employed by this study (Nakai et al., 2021). The subducting slab portion of HK1 underlies active focused fluid seepage detected using a combination of hydroacoustic, seafloor camera observations and geomorphological and seafloor acoustic backscatter data (Watson et al., 2019). This release of fluids also lies directly above and landward of subducted seamounts and on top of a high reflectivity zone (Bell et al., 2010). Bell et al. (2010) suggested that this high reflectivity zone is the result of a thick sedimentary package adjacent to the seamount. Both subducted seamounts and associated sediments could be important sources of fluids and, with their enhanced relief, subducted seamounts could generate the large splay faulting and fracturing observed in the overlying plate that facilitate the migration of fluids to the surface (Barker et al., 2018; Ellis et al., 2015; Wang & Bilek, 2011). Indeed, such faults have recently been observed in this area by seismic reflection data (Barker et al., 2018; Barnes et al., 2020). Additional fracturing adjacent to the subducted seamount in the underthrusting plate is supported by our relocated earthquakes that are concentrated in the downdip transition between this high Vp/Vs anomaly and moderate Vp/Vs (Figure 3).

This high Vp/Vs anomaly (HK1) may also provide insight into the SSEs in the northern Hikurangi margin. The portion of the plate that slipped during the 2014 SSE, shown on Figures 1, 4, and 5, lies directly on top of the well-resolved area of the HK1 anomaly (Figures 5, 9b, and 10). This correspondence between the 2014 SSE, the inferred subducted seamount (which likely leads to the large set of splay faulting in this region, Wang & Bilek, 2011), and high Vp/Vs ratios is consistent with the hypothesized high pore fluid pressures in this region. Intraslab seismicity near the SSE (Figures 3 and 6b) originating on faults within the slab points to deformation processes in the subducting oceanic crust. Seismicity spatially associated with subducted seamounts was also observed at slightly shallower depths using a repeating earthquake technique explored

by Shaddox and Schwartz (2019). These faults experience episodic changes in stress that facilitates build up and release of fluids into the overlying interface (Warren-Smith et al., 2019). Furthermore, splay faults in the upper plate were imaged in the vicinity of the HK1 anomaly through active seismic techniques (Barker et al., 2018; Bell et al., 2010), and have been found to play an important role in the permeability and dewatering paths of the fluids coming from deep subducted sediments (Ellis et al., 2015; Lauer & Saffer, 2012). The faulting and the subduction of fluid-rich unconsolidated sediments likely created the overpressured pore fluid conditions that enabled the onset of the 2014 SSE and perhaps the other SSEs events recorded over the last 20 years (Wallace, 2020).

Our Vp/Vs model shows strong heterogeneity with two high Vp/Vs anomalies (HK1 and HK2) separated by a zone with near-normal values of Vp/Vs ratios (1.73). This lateral variation is likely related to the uneven distribution of seamounts in the subducting plate, which may well explain the heterogeneous Vp/Vs structure. The presence of faults (mostly strike-slip and normal faults) is also likely nonuniform, as suggested by the distribution of earthquakes shown in Figure 3 and discussed in detail in Yarce et al. (2019). Additionally, the varying pressure and temperature conditions along dip in the subducting slab may contribute to the availability and migrations of fluids, affecting the subduction zone features such as the seismicity gap, variability of the Vp/Vs structure, and perhaps facilitating the onset of SSEs.

The distribution of earthquakes around high Vp/Vs segments of the subducting oceanic crust were also found within the oceanic crust of the subducting Philippine Sea Plate along the Nankai subduction margin (Akuhara et al., 2013). Recent seismic surveys over the Pacific Plate before subduction revealed a gradual increase of Vp/Vs toward the Japan Trench that can be ascribed to the hydration of the oceanic crust due to seawater penetration (Fujie et al., 2018). Obana et al. (2012) observed normal faulting seismicity aligned along the faults reaching the mantle of the Pacific Plate before subduction. Such faults are considered to act as fluid paths to the inner structure of the incoming plate. However, such hydration mechanism alone cannot explain the along-dip Vp/Vs partitioning within the oceanic crust of the subducting Hikurangi plateau. The Vp/Vs variation within the subducting slab may have been acquired at the time of its formation. More surveys and seismic observations over the incoming Hikurangi Plateau are needed to discuss the origin of the Vp/Vs variation in detail.

6. Conclusions

We have built 3D Vp and Vp/Vs tomographic models for the Hikurangi margin using local earthquakes recorded on OBSs as well as onshore data. Earthquake hypocenters reveal shallow seismicity distributed in two trench-parallel bands. The Vp model shows velocity gradients consistent with the outline of the plate interface, though smoother variations of P- velocities suggest a more diffuse plate boundary transition onshore. P wave velocity structure suggests that the thickness of the incoming oceanic crust ranges between 12 to 15 km, consistent with the subduction of an oceanic plateau. We found two high Vp/Vs anomalies, one offshore (HK1) in the subducting plate and down-dip from a known subducted seamount. A second high Vp/Vs anomaly (HK2) is located onshore around 20 km from HK1 and extending from the overlying plate into the upper portion of the subducted slab. The high Vp/Vs anomalies, along with earlier complementary geophysical studies, are interpreted as regions of high pore fluid pressures. These observations are consistent with the hypothesis that as the downgoing Hikurangi Plateau subducts beneath the North Island, fluid-rich sediments are accumulated down-dip from previously detected subducted seamounts. This subducting sedimentary package may supply high pore fluid pressures that, together with faulting and fracturing in the subducting slab, could facilitate slow slip of the plate and promote SSEs at shallow depths (Figure 10).

Data Availability Statement

References

Aki, K., & Richards, P. G. (1980). *Quantitative seismology*. University Science Books.

Akuhara, T., Mochizuki, K., Nakahigashi, K., Yamada, T., Shinohara, M., Sakai, S., et al. (2013). Segmentation of the Vp/Vs ratio and low-frequency earthquake distribution around the fault boundary of the Tonankai and Nankai earthquakes. *Geophysical Research Letters*, *40*(7), 1306–1310. https://doi.org/10.1002/grl.50223

Barker, D. H. N., Henrys, S., Caratori Tontini, F., Barnes, P. M., Bassett, D., Todd, E., & Wallace, L. (2018). Geophysical constraints on the relationship between seamount subduction, slow slip, and tremor at the North Hikurangi Subduction Zone, New Zealand. *Geophysical Research Letters*, *45*(23), 12804–12813. https://doi.org/10.1029/2018GL080259

Barnes, P. M., Wallace, L. M., Saffer, D. M., Bell, R. E., Underwood, M. B., Fagereng, A., et al. (2020). Slow slip source characterized by lithological and geometric heterogeneity. *Science Advances*, *6*. https://doi.org/10.1126/sciadv.aay3314

Bell, R., Sutherland, R., Barker, D. H. N., Henrys, S., Bannister, S., Wallace, L., & Beavan, J. (2010). Seismic reflection character of the Hikurangi subduction interface, New Zealand, in the region of repeated Gisborne slow slip events. *Geophysical Journal International*, *180*(1), 34–48. https://doi.org/10.1111/j.1365-246X.2009.04401.x

Berryman, J. G., Berge, P. A., & Bonner, B. P. (2002). Estimating rock porosity and fluid saturation using only seismic velocities. *Geophysics*, *67*(2), 391–404. https://doi.org/10.1190/1.1468599

Brantut, N., & David, E. C. (2019). Influence of fluids on VP/VS ratio: Increase or decrease? *Geophysical Journal International*, *216*(3), 2037–2043. https://doi.org/10.1093/gji/ggy518

Bürgmann, R. (2018). The geophysics, geology and mechanics of slow fault slip. *Earth and Planetary Science Letters*, *495*, 112–134. https://doi.org/10.1016/j.epsl.2018.04.062

Christensen, N. I. (1984). Pore pressure and oceanic crustal seismic structure. *Geophysical Journal International*, *79*, 411–423. https://doi.org/10.1111/j.1365-246X.1984.tb02232.x

Comte, D., Farias, M., Roecker, S., & Russo, R. (2019). The nature of the subduction wedge in an erosive margin: Insights from the analysis of aftershocks of the 2015 Mw 8.3 Illapel earthquake beneath the Chilean Coastal Range. *Earth and Planetary Science Letters*, *520*, 50–62. https://doi.org/10.1016/j.epsl.2019.05.033

Condie, K. C. (2016). The crust. In Earth as an evolving planetary system (pp. 9–41). https://doi.org/10.1016/b978-0-12-803689-1.00002-x

Davy, B., Hoernle, K., Werner, R., & Werner, R. (2008). Hikurangi Plateau: Crustal structure, rifted formation, and Gondwana subduction history. *Geochemistry, Geophysics, Geosystems*, *9*(7), Q07004. https://doi.org/10.1029/2007GC001855

Eberhart-Phillips, D., & Bannister, S. (2015). 3-D imaging of the northern Hikurangi subduction zone, New Zealand: Variations in subducted sediment, slab fluids and slow slip. *Geophysical Journal International*, *201*(2), 838–855. https://doi.org/10.1093/gji/ggv057

Ellis, S., Fagereng, Å., Barker, D., Henrys, S., Saffer, D., Wallace, L., et al. (2015). Fluid budgets along the northern Hikurangi subduction margin, New Zealand: The effect of a subducting seamount on fluid pressure. *Geophysical Journal International*, *202*(1), 277–297. https://doi.org/10.1093/gji/ggv127

Fujie, G., Kodaira, S., Kaiho, Y., Yamamoto, Y., Takahashi, T., Miura, S., & Yamada, T. (2018). Controlling factor of incoming plate hydration at the north-western Pacific margin. *Nature Communications*, *9*(1), 1–7. https://doi.org/10.1038/s41467-018-06320-z

Gray, M., Bell, R. E., Morgan, J. V., Henrys, S., & Barker, D. H. N. (2019). Imaging the shallow subsurface structure of the North Hikurangi subduction zone, New Zealand, using 2-D full-waveform inversion. *Journal of Geophysical Research: Solid Earth*, *124*(8), 9049–9074. https://doi.org/10.1029/2019JB017793

Greenfield, T., White, R. S., & Roecker, S. (2016). The magmatic plumbing system of the Askja central volcano, Iceland, as imaged by seismic tomography. *Journal of Geophysical Research: Solid Earth*, *121*(10), 7211–7229. https://doi.org/10.1002/2016JB013163

Haijima, D. (2015). *Seismic activity and velocity structure in the Northern Hikurangi subduction zone offshore the north Island of New Zealand. Earthquake research institute, department of Earth and planetary science*. University of Tokyo

Heise, W., Caldwell, T. G., Bannister, S., Bertrand, E. A., Ogawa, Y., Bennie, S. L., & Ichihara, H. (2017). Mapping subduction interface coupling using magnetotellurics: Hikurangi margin, New Zealand. *Geophysical Research Letters*, *44*(18), 9261–9266. https://doi.org/10.1002/2017GL074641

Hole, J. A., & Zelt, B. C. (1995). 3-D finite-difference reflection travel times. *Geophysical Journal International*, *121*(2), 427–434. https://doi.org/10.1111/j.1365-246X.1995.tb05723.x

Ito, Y., Obara, K., Shiomi, K., Sekine, S., & Hirose, H. (2007). Slow earthquakes coincident with episodic tremors and slow slip events. *Science*, *315*(5811), 503–506. https://doi.org/10.1126/science.1134454

Kerr, A. C. (2003). Oceanic plateaus, In Treatise on geochemistry (Vol. 3–9, pp. 537–565). Pergamon. https://doi.org/10.1016/B0-08-043751-6/03033-4

Kodaira, S., Iidaka, T., Kato, A., Park, J.-O. O., Iwasaki, T., & Kaneda, Y. (2004). High pore fluid pressure may cause silent slip in the Nankai Trough. *Science*, *304*(5675), 1295–1298. https://doi.org/10.1126/science.1096535

Lauer, R. M., & Saffer, D. M. (2012). Fluid budgets of subduction zone forearcs: The contribution of splay faults. *Geophysical Research Letters*, *39*(13), L13604. https://doi.org/10.1029/2012GL052182

Li, Z., Roecker, S., Li, Z., Bin, W., Haitao, W., Schelochkov, G., & Bragin, V. (2009). Tomographic image of the crust and upper mantle beneath the western Tien Shan from the MANAS broadband deployment: Possible evidence for lithospheric delamination. *Tectonophysics*, *477*(1–2), 49–57. https://doi.org/10.1016/j.tecto.2009.05.007

Mochizuki, K., Sutherland, R., Henrys, S., Bassett, D., Van Avendonk, H., Arai, R., et al. (2019). Recycling of depleted continental mantle by subduction and plumes at the Hikurangi Plateau large igneous province, southwestern Pacific Ocean. *Geology*, *47*(8), 795–798. https://doi.org/10.1130/G46250.1

Mochizuki, K., Yamada, T., Shinohara, M., Yamanaka, Y., & Kanazawa, T. (2008). Weak interplate coupling by seamounts and repeating M 7 earthquakes. *Science*, *321*(5893), 1194–1197. https://doi.org/10.1126/science.1160250

Mooney, W. D., Laske, G., & Masters, T. G. (1998). CRUST 5.1: A global crustal model at 5° × 5°. *Journal of Geophysical Research*, *103*(1), 727–747. https://doi.org/10.1029/97jb02122

Nakai, J. S., Sheehan, A. F., Abercrombie, R. E., & Eberhart-Phillips, D. (2021). Near trench 3D seismic attenuation offshore Northern Hikurangi subduction margin, North Island, New Zealand. *Journal of Geophysical Research: Solid Earth*, *126*(3), e2020JB020810. https://doi.org/10.1029/2020JB020810

O'Connell, R. J., & Budiansky, B. (1974). Seismic velocities in dry and saturated cracked solids. *Journal of Geophysical Research*, *79*(35), 5412–5426. https://doi.org/10.1029/jb079i035p05412

Obana, K., Fujie, G., Takahashi, T., Yamamoto, Y., Nakamura, Y., Kodaira, S., et al (2012). Normal-faulting earthquakes beneath the outer slope of the Japan Trench after the 2011 Tohoku earthquake: Implications for the stress regime in the incoming Pacific plate. *Geophysical Research Letters*, *39*(7), L00G24. https://doi.org/10.1029/2011GL050399

Paige, C. C., & Saunders, M. A. (1982). LSQR: An algorithm for sparse linear equations and sparse least squares. *ACM Transactions on Mathematical Software*, *8*(1), 43–71. https://doi.org/10.1145/355984.355989

Prevot, R., Hatzfeld, D., Roecker, S. W., & Molnar, P. (1980). Shallow earthquakes and active tectonics in eastern Afghanistan. *Journal of Geophysical Research*, *85*(B3), 1347–1357. https://doi.org/10.1029/JB085iB03p01347

Rawlinson, N., Fichtner, A., Sambridge, M., & Young, M. K. (2014). Seismic Tomography and the Assessment of Uncertainty. *Advances in Geophysics*, *55*, 1–76. https://doi.org/10.1016/bs.agph.2014.08.001

Rawlinson, N., & Spakman, W. (2016). On the use of sensitivity tests in seismic tomography. *Geophysical Journal International*, *205*, 1221–1243. https://doi.org/10.1093/gji/ggw084

Roecker, S., Ebinger, C., Tiberi, C., Mulibo, G., Ferdinand-Wambura, R., Mtelela, K., et al. (2017). Subsurface images of the Eastern Rift, Africa, from the joint inversion of body waves, surface waves and gravity: Investigating the role of fluids in early-stage continental rifting. *Geophysical Journal International*, *210*(2), 931–950. https://doi.org/10.1093/gji/ggx220

Roecker, S., Thurber, C., Roberts, K., & Powell, L. (2006). Refining the image of the San Andreas Fault near Parkfield, California using a finite difference travel time computation technique. *Tectonophysics*, *426*(1–2), 189–205. https://doi.org/10.1016/J.TECTO.2006.02.026

Schuler, J., Greenfield, T., White, R. S., Roecker, S. W., Brandsdóttir, B., Stock, J. M., et al. (2015). Seismic imaging of the shallow crust beneath the Krafla central volcano, NE Iceland. *Journal of Geophysical Research: Solid Earth*, *120*(10), 7156–7173. https://doi.org/10.1002/2015JB012350

Shaddox, H. R., & Schwartz, S. Y. (2019). Subducted seamount diverts shallow slow slip to the forearc of the northern Hikurangi subduction zone, New Zealand. *Geology*, *47*, 415–418. https://doi.org/10.1130/g45810.1

Stern, T., Stratford, W., Seward, A., Henderson, M., Savage, M., Smith, E., et al. (2010). Crust-mantle structure of the central North Island, New Zealand, based on seismological observations. *Journal of Volcanology and Geothermal Research*, *190*(1–2), 58–74. https://doi.org/10.1016/J.JVOLGEORES.2009.11.017

Sun, T., Saffer, D., & Ellis, S. (2020). Mechanical and hydrological effects of seamount subduction on megathrust stress and slip. *Nature Geoscience*, *13*(3), 249–255. https://doi.org/10.1038/s41561-020-0542-0

Todd, E. K., Schwartz, S. Y., Mochizuki, K., Wallace, L. M., Sheehan, A. F., Webb, S. C., et al. (2018). Earthquakes and Tremor linked to seamount subduction during shallow slow slip at the Hikurangi Margin, New Zealand. *Journal of Geophysical Research: Solid Earth*, *123*(8), 6769–6783. https://doi.org/10.1029/2018JB016136

Vidale, J. (1988). Finite-difference calculation of travel times. *Bulletin Seismological Society of America*, *78*(6), 2062–2076.

Wallace, L. M. (2020). Slow slip events in New Zealand. *Annual Review of Earth and Planetary Sciences*, *48*(1), 175–203. https://doi.org/10.1146/annurev-earth-071719-055104

Wallace, L. M., Beavan, J., McCaffrey, R., & Desmond, D. (2004). Subduction zone coupling and tectonic block rotations in the North Island, New Zealand. *Journal of Geophysical Research*, *109*(B12), B12406. https://doi.org/10.1029/2004JB003241

Wallace, L. M., Kaneko, Y., Hreinsdóttir, S., Hamling, I., Peng, Z., Bartlow, N., et al. (2017). Large-scale dynamic triggering of shallow slow slip enhanced by overlying sedimentary wedge. *Nature Geoscience*, *10*(10), 765–770. https://doi.org/10.1038/ngeo3021

Wallace, L. M., Webb, S. C., Ito, Y., Mochizuki, K., Hino, R., Henrys, S., et al. (2016). Slow slip near the trench at the Hikurangi subduction zone, New Zealand. *Science*, *352*(6286), 701–704. https://doi.org/10.1126/science.aaf2349

Wang, K., & Bilek, S. L. (2011). Do subducting seamounts generate or stop large earthquakes? *Geology*, *39*(9), 819–822. https://doi.org/10.1130/G31856.1

Warren-Smith, E., Fry, B., Wallace, L., Chon, E., Henrys, S., Sheehan, A., et al. (2019). Episodic stress and fluid pressure cycling in subducting oceanic crust during slow slip. *Nature Geoscience*, *12*(6), 475–481. https://doi.org/10.1038/s41561-019-0367-x

Watson, S. J., Mountjoy, J. J., Barnes, P. M., Crutchley, G. J., Lamarche, G., Higgs, B., et al. (2019). Focused fluid seepage related to variations in accretionary wedge structure, Hikurangi margin, New Zealand. *Geology*, *48*, 56–61. https://doi.org/10.1130/G46666.1

Williams, C. A., Eberhart-Phillips, D., Bannister, S., Barker, D. H. N., Henrys, S., Reyners, M., & Sutherland, R. (2013). Revised interface geometry for the Hikurangi subduction zone, New Zealand. *Seismological Research Letters*, *84*(6), 1066–1073. https://doi.org/10.1785/0220130035

Yarce, J., Sheehan, A. F., Nakai, J. S., Schwartz, S. Y., Mochizuki, K., Savage, M. K., et al. (2019). Seismicity at the Northern Hikurangi Margin, New Zealand, and investigation of the potential spatial and temporal relationships with a shallow slow slip event. *Journal of Geophysical Research: Solid Earth*, *124*(5), 4751–4766. https://doi.org/10.1029/2018JB017211

Zal, H. J., Jacobs, K., Savage, M. K., Yarce, J., Mroczek, S., Graham, K., et al. (2020). Temporal and spatial variations in seismic anisotropy and V/V ratios in a region of slow slip. *Earth and Planetary Science Letters*, *532*, 115970. https://doi.org/10.1016/j.epsl.2019.115970

Zhang, H., Roecker, S. H. C., & Wang, W. (2012). *Seismic imaging of microblocks and weak zones in the crust beneath the Southeastern margin of the Tibetan plateau*. Earth Sciences.